Geosciences 2026, 12(1): 1-20
DOI: 10.5923/j.geo.20261201.01

# Source Mechanism and Regional Stress Field of the 2025 Mw 7.7 Myanmar Earthquake: Evidence for Active Deformation in the Indo-Myanmar Range

**Khundrkpam Kumarjit Singh*, Soibam Ibotombi, Sanoujam Manichandra, Lamnganba Thokchom, Thokchom Nilamani Singh**

Department of Earth Sciences, Manipur University, Imphal, Manipur, India

**Abstract** The Mw 7.7 Myanmar earthquake of 28 March 2025, which ruptured the active Sagaing Fault, provides a unique opportunity to investigate the seismotectonic processes governing deformation along the India–Sunda plate boundary and within the Indo-Myanmar Range (IMR). Here, we present an independent focal mechanism solution derived from 395 P-wave first-motion polarity observations compiled from the International Seismological Centre (ISC) bulletin and evaluate it against the published United States Geological Survey (USGS) solution. The preferred solution comprises two near-vertical nodal planes (001°/89° and 265°/89°), indicating predominantly dextral strike-slip faulting with a minor normal-faulting component. Correlation of the N-S trending nodal plane with the mapped trace of the Sagaing Fault identifies it as the causative rupture plane, while the close agreement with the USGS solution validates the robustness of the independently derived mechanism. Integration of the focal mechanism with regional geological and geodetic constraints demonstrates that the Sagaing Fault accommodates a substantial proportion of the relative motion between the Indian and Sunda plates, emphasizing its key role in strain partitioning across the obliquely convergent plate boundary. The derived stress field is characterized by NE–SW compression and NW–SE extension, reflecting the regional kinematics of the India–Sunda plate interaction. The northwest-directed extensional component exerts a westward tectonic push on the Indo-Myanmar Range, generating E–W compression and N–S extension, consistent with the present-day deformation pattern inferred from geological structures and geodetic observations. These results provide new constraints on the rupture mechanics of the 2025 Myanmar earthquake and advance our understanding of stress partitioning, active fault kinematics, and continental deformation within one of the world's most tectonically active oblique plate boundaries.

**Keywords** Sagaing Fault, Focal Mechanism, First-Motion Polarity, Regional Stress Field, Indo–Myanmar Ranges

## 1. Introduction

Myanmar occupies a pivotal position at the junction of the Indian, Eurasian, and Sunda plates, forming one of the most tectonically complex and seismically active regions within the Alpine–Himalayan orogenic system. This tectonic setting accommodates the ongoing convergence of the Indian Plate with Southeast Asia through a combination of continental collision, oblique subduction, strike-slip faulting, and distributed crustal deformation. Consequently, Myanmar represents a natural laboratory for investigating the interplay between plate kinematics, active faulting, and continental deformation, while simultaneously facing one of the highest levels of seismic hazard in Southeast Asia.

Geographically, Myanmar extends for nearly 2,000 km from approximately 10°N to 28°N and is bounded by India, Bangladesh, the Bay of Bengal and Andaman Sea to the west, and China, Laos, and Thailand to the east. The country exhibits remarkable physiographic diversity, consisting of a central lowland corridor bordered by prominent north–south -trending mountain belts. To the west, the Patkai Range, Naga Hills, Chin Hills, and Rakhine Yoma constitute the eastern margin of the Indo-Burma Ranges, whereas the Shan Plateau dominates the eastern highlands with an average elevation of about 900 m. The central depression is traversed by the Ayeyarwaddy, Chindwin, Thanlwin, and Sittaung river systems, which collectively drain southward into the Andaman Sea and the Gulf of Mottama. The Bago Yoma separates the Ayeyarwaddy and Sittaung basins and extends northward into a chain of extinct volcanic centres, including Mount Popa. Climatically, Myanmar lies within the Asian monsoon belt and experiences pronounced seasonal variations, with topography exerting a strong control on regional

* Corresponding author:
khkumarjitsingh1@gmail.com (Khundrkpam Kumarjit Singh)
Received: Jul. 20, 2026; Accepted: Aug. 9, 2026; Published: Aug. 13, 2026
Published online at http://journal.sapub.org/geo

precipitation and contributing to recurrent natural hazards, including destructive tropical cyclones along its western coastline.

The active tectonics of Myanmar are primarily controlled by the oblique convergence between the Indian Plate and the Burma Microplate, together with the relative motion between the Burma and Sunda plates. This deformation is partitioned between eastward subduction of the Indian Plate beneath the Indo-Burma Ranges and dextral strike-slip motion along the Sagaing Fault, a major lithospheric-scale transform fault extending for approximately 1,400 km through central Myanmar. The Sagaing Fault accommodates a substantial proportion of the northward motion of the Burma Microplate relative to the Sunda Plate and has generated numerous destructive historical earthquakes, making it one of the most significant active continental strike-slip faults in Southeast Asia.

On 28 March 2025, central Myanmar experienced a catastrophic moment magnitude (Mw) 7.7 earthquake that ruptured a major segment of the Sagaing Fault (Figure 1). The earthquake represents the largest and most destructive seismic event in Myanmar in more than a century. The rupture nucleated within a previously recognized seismic gap and propagated over approximately 460 km, with portions of the rupture exhibiting supershear propagation. The shallow focal depth (~10 km) generated surface displacements locally exceeding 6 m and was followed within minutes by a Mw 6.7 aftershock together with an extensive aftershock sequence. The earthquake produced severe ground shaking, reaching Modified Mercalli Intensity IX across Mandalay, Sagaing, and Naypyidaw, while its effects were felt throughout neighbouring countries, including Thailand. Amplification of seismic waves within the unconsolidated sediments of the Central Myanmar Basin, together with widespread liquefaction and the vulnerability of existing infrastructure, significantly intensified the damage. The event resulted in more than 4,900 fatalities, thousands of injuries, and extensive destruction of residential buildings, public infrastructure, and culturally significant monuments. Beyond its humanitarian consequences, the earthquake highlighted the urgent need to improve seismic hazard assessment, earthquake-resistant design, and regional disaster preparedness throughout Myanmar and adjoining regions.

Despite the exceptional scientific significance of this earthquake, several fundamental questions remain regarding its rupture characteristics, source parameters, and implications for the regional stress regime governing deformation across the Indo-Burma plate boundary. Although rapid source solutions released by international agencies, including the United States Geological Survey (USGS), provide valuable first-order constraints, independent determinations based on teleseismic observations are essential for validating fault geometry, rupture kinematics, and regional tectonic interpretations. Such analyses contribute to a more robust understanding of active deformation processes and provide critical constraints for future seismic hazard assessments.

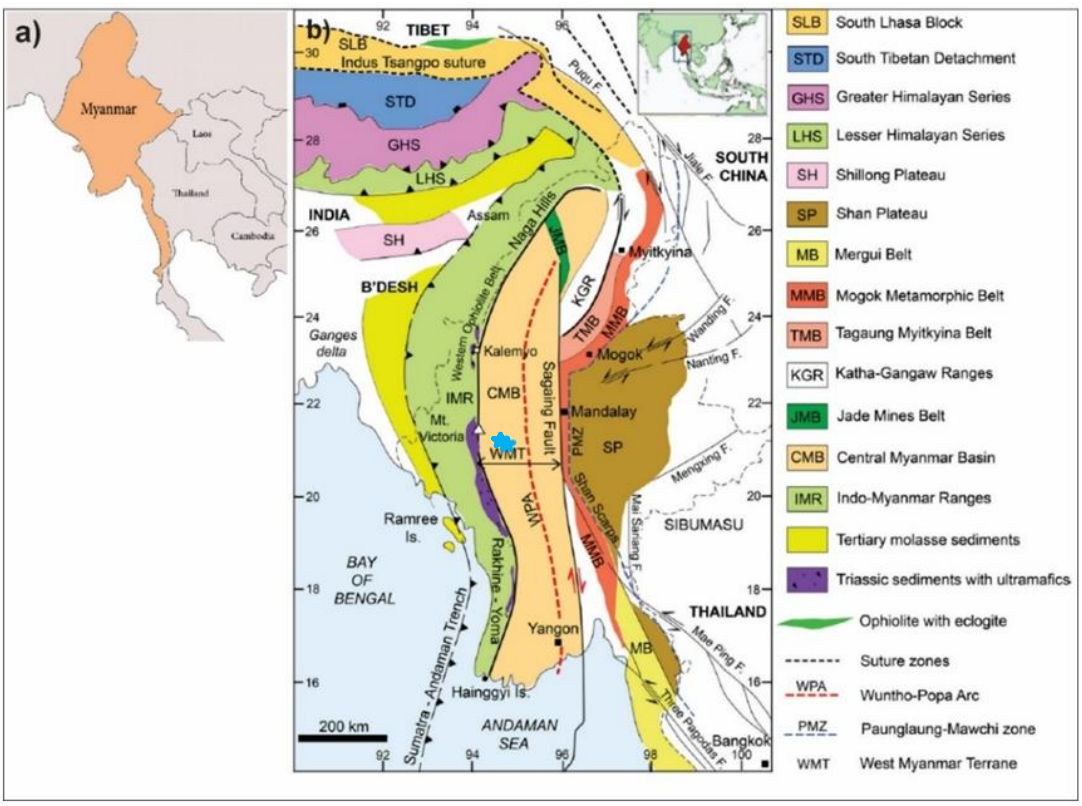


**Figure 1.** a) Location map of Myanmar in Southeast Asia. b) Simplified geological map of Myanmar (Burma) from the eastern Himalayan Syntaxis south to Mergui. Source: modified after [1]

In this study, we present an independent seismotectonic investigation of the 28 March 2025 Mw 7.7 Myanmar earthquake by integrating teleseismic waveform analysis, P-wave first-motion polarity data, focal mechanism inversion, and regional geological information. The independently derived focal mechanism is compared with the published USGS solution to evaluate the consistency of fault-plane geometry and rupture kinematics. In addition, key source parameters, including moment magnitude, focal depth, and epicentral distance, are estimated and interpreted within the framework of the regional tectonic setting. Finally, the implications of the earthquake for the contemporary stress field, fault interactions, and deformation mechanisms operating along the Indo-Burma–Sunda plate boundary are examined. The results provide new insights into the geodynamics of one of the world's most active oblique plate boundaries and contribute to a better understanding of earthquake generation processes in the Indo-Myanmar region.

## 2. Geological and Tectonic Setting

Myanmar lies at the complex junction of the Indian, Eurasian, and Sunda plates, where ongoing oblique convergence drives intense tectonic deformation. This geodynamic setting has produced a network of active fault systems, notably the north–south trending Sagaing Fault, which accommodates significant right-lateral strike-slip motion between the Burma Microplate and the Sunda Plate. On 28 March 2025, a Mw 7.7 earthquake ruptured the central and southern segments of the Sagaing Fault, severely affecting Sagaing, Mandalay, and Nay Pyi Taw. The tectonic environment is further influenced by the oblique subduction of the Indian Plate beneath the Burma Microplate along the Indo-Myanmar Ranges to the west, and the collision of the Indian Plate with the Eurasian Plate to the north. This interplay of strike-slip faulting, subduction processes, and continental collision makes Myanmar one of Southeast Asia’s most seismically active regions, where large earthquakes pose significant hazards to densely populated and rapidly urbanizing areas.

### 2.1. Geological and Tectonic Setting of Myanmar

Myanmar occupies a critical tectonic position at the northeastern margin of the Indian Plate, where active oblique convergence with the Eurasian and Sunda plates has created a structurally complex and seismically active region [2,3,4]. This interaction, initiated in the Eocene, involves multiple lithospheric elements—the Indian Plate, the Burma (Myanmar) Microplate, the Shan–Thai Block, and the Sunda Plate—separated by a network of major fault systems. The present-day tectonic configuration results from the prolonged convergence and differential motion of these blocks, forming three distinct north–south-trending geotectonic domains: (1) the Indo-Myanmar (Burma) Ranges (IMR) to the west, (2) the Central Myanmar Basin (CMB), and (3) the Shan Plateau to the east (Figure 1). These domains exhibit a characteristic westward convex arcuate geometry and are bounded to the north by the Eastern Himalayan Syntaxis [2,5,6].

**Indo-Myanmar (Burma) Ranges (IMR)**

The Indo-Burma Ranges constitute a ~1,300 km long arcuate fold–thrust belt that extends from the Eastern Himalayan Syntaxis in northeast India through western Myanmar into Bangladesh and continues southward beneath the Andaman Sea, re-emerging as the Andaman–Nicobar Islands [7]. The IMR developed as an accretionary prism during Late Cretaceous–Early Eocene subduction along the eastern margin of the Neotethys, subsequently evolving into a subaerial fold–thrust system following collision between the Indian Plate and the Southeast Asian margin in the Late Eocene [8,2,3]. The belt is presently underlain by an active east-dipping subduction zone that generates frequent intermediate-depth seismicity [9,10].

Structurally, the IMR is segmented by several faults including the Kabaw Fault on the eastern flank and internal strike-slip faults such as the Kaladan, Kheng, and Lelon Faults [2,11]. Internally, the belt is subdivided into Outer, Inner, and Eastern belts based on lithology and structural complexity. The Outer Belt consists primarily of Neogene sediments, while the Inner Belt includes Upper Cretaceous to Paleogene flysch sequences. The Eastern Belt exposes structurally complex assemblages containing ophiolitic fragments, serpentinites, cherts, and metamorphosed oceanic units [12,13,14].

Ophiolitic complexes—such as those at Kalemyo (Myanmar) and in Nagaland-Manipur (India)—are key indicators of ancient oceanic lithosphere emplacement. These bodies, often dismembered, include serpentinized peridotites, diabases, pillow basalts, and associated radiolarian cherts embedded in sheared mélanges [15,16,13]. Some, such as the Webula peridotite, are thrust over sedimentary units along east-dipping basal faults, accompanied by metamorphic soles indicative of supra-subduction zone ophiolite emplacement [5].

Deformation in the IMR is multiphase: initial subduction-accretion processes were followed by collision-driven folding and thrusting, later overprinted by dextral strike-slip faulting during the Neogene [5]. The overall westward convex geometry of the range, especially pronounced near 22°N, reflects kinematic partitioning due to oblique convergence and lateral extrusion of crustal blocks [6,1].

### 2.2. Central Myanmar Basin (CMB)

Situated between the IMR and the Sagaing Fault, the Central Myanmar Basin comprises a series of Cenozoic forearc and backarc sub-basins—Hukwang, Chindwin, Shwebo, Salin (Minbu), Pyay, Irrawaddy Delta, Bago Yoma, and Sittaung. These basins accommodate up to 18 km of sedimentary fill, documenting the region’s tectonostratigraphic evolution from marine to continental environments [17].

The basin architecture preserves evidence of multiple deformation episodes, as revealed by four basin-wide unconformities—dated to the Late Cretaceous, Late Eocene, Oligocene, and Late Miocene—corresponding to changes in tectonic regime [18]. Stratigraphically, the basin begins with the Albian–Maastrichtian Kabaw Formation (marine siliciclastics and carbonates), overlain by fluvio-deltaic Paleocene–Eocene units (e.g., Paunggyi, Pondaung, Yaw formations), followed by the Shwezetaw, Padaung, and Okhmintaung formations of Oligocene–Miocene age. The uppermost Pyawbwe to Irrawaddy formations represent molassic deposits accumulated during basin inversion associated with Himalayan orogenesis and regional uplift [19,20].

Tectonically, these basins experienced Miocene dextral transtension followed by Pliocene–Pleistocene transpression, as indicated by strike-slip faults, oblique-reverse faults, and fault-propagation folds [6,18]. The thick, unconsolidated sedimentary sequences increase susceptibility to ground motion amplification and liquefaction during large earthquakes, as observed during the 28 March 2025 Mw 7.7 event.

### 2.3. Sagaing Fault Zone

The Sagaing Fault is a ~1,400 km long right-lateral strike-slip fault that forms the principal boundary between the Burma Microplate and the Sunda Plate. It extends from the Andaman Sea Spreading Center in the south to the Eastern Himalayan Syntaxis in the north and accommodates 18–24 mm/yr of relative plate motion [21,22,23]. Displacement estimates since the Miocene range from 100 to 450 km [24,25].

The fault exhibits classic strike-slip morphotectonic features including linear valleys, offset drainages, sag ponds (e.g., Yega Inn), and pull-apart basins such as Indawgyi Lake. GPS and InSAR studies indicate segment-specific variations in slip rates and locking depths (10–16 km), with central and southern segments exhibiting strain accumulation consistent with potential Mw 7.3–7.4 earthquakes [26].

Petrological and structural studies reveal brecciated serpentinites, fault gouge zones, and high-strain mylonitic rocks, particularly within the Sagaing Metamorphic (SM) and Minwun Metamorphic (MM) belts, indicating intense shearing and high-temperature ductile deformation along the fault core [1]. The SM unit includes hornblende gneiss, amphibolite, and granulite-facies rocks dated to ~21 Ma, reflecting early ductile deformation, while the MM unit contains greenschist- to amphibolite-grade rocks reflecting later overprinting.

### 2.4. Shan Plateau and Mogok Metamorphic Belt (MMB)

East of the Sagaing Fault lies the Shan Plateau, a high-standing (~1,000 m elevation) terrane underlain by thick Proterozoic to Mesozoic sedimentary sequences. Deformation in the plateau involves folding, thrusting, and crustal uplift associated with the India–Asia collision and lateral escape tectonics [1,4].

Separating the plateau from the CMB, the Mogok Metamorphic Belt (MMB) extends over 1,500 km and is composed of high-grade marbles, garnet-bearing schists, and gneisses intruded by granitic pegmatites. These rocks exhibit strong ductile fabrics—sheath folds, stretching lineations, and foliation development—suggesting deep crustal deformation and crustal extrusion [5]. Radiometric dating constrains MMB deformation to pre-Sagaing Fault activity, likely linked to earlier Himalayan orogeny events.

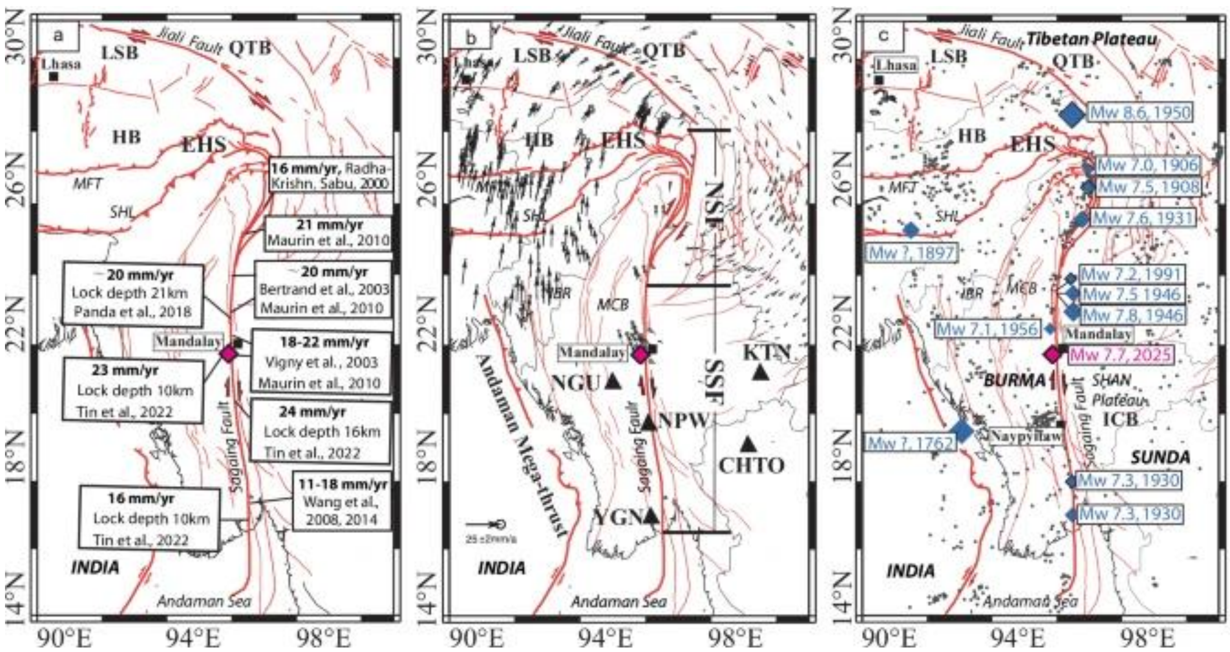


**Figure 2.** Fault geometry, kinematics, and historical seismicity along the Sagaing Fault Zone. (a) Map showing major active faults and estimated right-lateral slip rates along the Sagaing Fault, compiled from [27,28,29]. (b) GPS velocity field relative to the South China Block, based on data from [30,31]. Black triangles indicate locations of strong-motion stations. NSF: North Sagaing Fault; SSF: South Sagaing Fault. (c) Seismicity distribution along the fault. Gray dots represent earthquake hypocenters from [32] and the USGS catalog. Blue diamonds mark epicenters of historical earthquakes with magnitude ≥ 7 (ISC catalog). The red diamond denotes the epicenter of the March 28, 2025 Mw 7.7 earthquake. IBR: Indo-Burma Ranges; MCB: Myanmar Central Basin; SHL: Shillong Plateau; HFT: Himalayan Frontal Thrust

Myanmar's tectonic architecture results from a prolonged history of subduction, collision, and strike-slip faulting along an evolving convergent margin. The Indo-Burma Ranges represent an accretionary wedge above an active subduction zone, the Central Myanmar Basin preserves forearc to backarc stratigraphy with multiple tectonic inversions, and the Sagaing Fault accommodates major intra-plate dextral motion. Eastward, the Shan Plateau and MMB record high-grade metamorphism and ductile deformation linked to continental collision and extrusion. Together, these domains constitute a highly active geodynamic system, where ongoing deformation poses significant seismic hazards, exemplified by the recent Mw 7.7 earthquake of 28 March 2025.

# 3. Methodology

## 3.1. Data Collection

Seismic first-motion data for the 28 March 2025 Myanmar earthquake were obtained from the International Seismological Centre (ISC) bulletin. A total of 395 polarity observations were compiled (Appendix), including station identifiers, epicentral distances, azimuths, P-wave arrival times, and first-motion polarities that are classified as compression (c) —upward first motion, or dilation (d) —downward first motion [33,34,35].

## 3.2. Focal Mechanism Construction

The focal mechanism solution was derived using first-motion polarity analysis [36,37]. For each station, the azimuth and polarity were used to classify the P-wave as compressional or dilatational. Data plotting and nodal plane construction were performed on a lower-hemisphere, equal-area stereographic projection (Schmidt net) using a transparent overlay. The primitive circle and cardinal directions (N, S, E, W) were first delineated for reference. Station positions were plotted according to their azimuths, with compressional arrivals marked by solid circles (•) and dilatational arrivals by open circles (○).

Two nodal planes, representing the fault plane and its auxiliary, were constructed to optimally separate the compressional and dilatational quadrants, thereby forming four distinct regions. The orientations of these planes were measured directly from the stereonet as:

- Fault Plane 1: Strike = 265°, Dip = 89° N
- Fault Plane 2: Strike = 001°, Dip = 89° E

The principal stress axes were derived from the two nodal planes of the focal mechanism. The intersection of the nodal planes defines the orientation of the intermediate principal stress axis ($\sigma_2$). A great circle perpendicular to $\sigma_2$ was then constructed. Within the dilation quadrant, the angle between the two nodal planes was measured, and its bisector was taken to define the orientation of the maximum principal stress axis ($\sigma_1$). The minimum principal stress axis ($\sigma_3$) was subsequently located along the same great circle at a position 90° from $\sigma_1$.

# 4. Result

## 4.1. Focal Mechanism Solution

We derived the strike, dip, and rake angles of the March 28, 2025 Myanmar earthquake. A comparison is made between the focal mechanism solution derived in this study and that published by the United States Geological Survey (USGS). Here, the construction of the focal mechanism of the 2025 Myanmar earthquake using the polarity data from the International Seismological Centre (ISC) bulletin is consistent with the published mechanism available on the USGS website, with minor variation in the orientation of three principal stresses. Since the orientation of $\sigma_2$, the intermediate principal stress, is vertical, the main controlling mechanism of this earthquake is a strike-slip faulting mechanism with a minor component of gravity faulting. Among the two nodal planes, the actual faulting that caused the 2025 Myanmar earthquake is the one trending N-S, having the attitude - 001°/89° E, because the epicenter falls on the Sagaing fault, which trends N-S with dextral strike-slip motion as represented by the fault plane solution shown in Figure 3. This fault geometry has been further supported by the results of the first aftershock event: Mw 6.7; 28 March 2025, 06:32:04 UTC (cf: USGS website), which exhibits a remarkably similar fault geometry (NP1: Strike = 81°, Dip = 82°, Rake = −34°; NP2: Strike = 177°, Dip = 56°, Rake = −170°).

**Table 1.** Values of the nodal planes and the corresponding orientation of the three principal stresses for both the present study and the one published in USGS

| | Nodal Planes | | | | Principal Axes | | | Faulting Mechanism | Kagan Angle Relative to USGS |
|---|---|---|---|---|---|---|---|---|---|
| | **Plane** | **Strike** | **Dip** | **Rake** | **Axis** | **Plunge** | **Azimuth** | | |
| **USGS** | **NP1** | 1° | 82° | -174° | $\sigma_3$ | 1° | 315° | Strike-Slip | _ |
| | **NP2** | 270° | 84° | -8° | $\sigma_2$ | 80° | 52° | | |
| | | | | | $\sigma_1$ | 10° | 225° | | |
| **Present Study** | **NP1** | 1° | 89° | -179° | $\sigma_3$ | 1° | 313° | Strike-Slip | 8.6° |
| | **NP2** | 265° | 89° | -5° | $\sigma_2$ | 88° | 43° | | |
| | | | | | $\sigma_1$ | 2° | 222° | | |

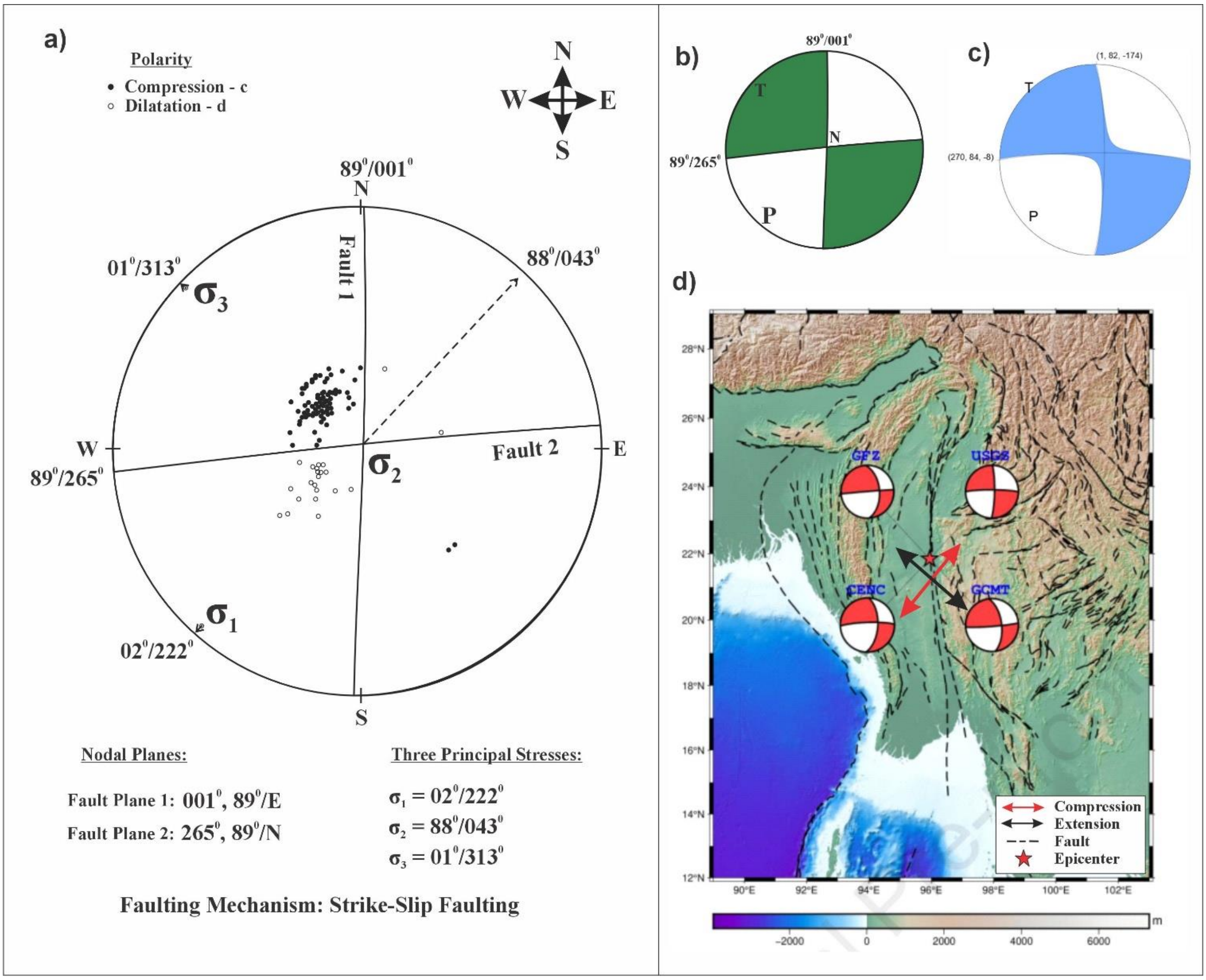


**Figure 3.** a) Focal mechanism solution of the 28th of March 2025 Myanmar Earthquake showing the two nodal planes: Fault 1 - 001°,89°/E and Fault 2 - 265°,89°/N characterizing sinistral and dextral strike-slip motion respectively. b) Beach-ball representation of the said earthquake corresponds to Figure (a). c) Earthquake beach ball generated from USGS for comparison. d) Map showing NE-SW compression (red double-headed arrow) and NW-SE extension (black double-headed arrow) field at the earthquake site where the extension component gives a westerly push to the IMR

### 4.2. Kagan Angle

To verify the accuracy of the focal mechanism solutions obtained, we collected the results provided by several internationally authoritative institutions in the field of seismology and used the Kagan angle [38,39] to measure the differences between the present solutions and those results of the USGS. The Kagan angle is a key indicator for measuring the similarity or difference between the two focal mechanism solutions. It comprehensively considers various parameters of the focal mechanism solutions, such as the strike, dip angle, and rake of the nodal planes, and then converts the differences in these parameters into a single angular value. This conversion makes a comparison between different focal mechanism solutions more intuitive and convenient. For example, if the Kagan angle between two focal mechanism solutions is 0°, it indicates that they are completely identical; conversely, the larger the Kagan angle, the more significant the difference between the two focal mechanism solutions.

Figure 3d presents the focal mechanisms of the 2025 Myanmar earthquake determined by different agencies. The strike, dip, and rake of the two nodal planes provided by the China Earthquake Networks Center (CENC) are 268/82/-32 and 3/58/-170, respectively. The focal mechanism solution results from three institutions, namely the United States Geological Survey (USGS), the German Research Centre for Geosciences (GFZ), and the Global Centroid Moment Tensor (GCMT), are presented in Table 2.

The Kagan angles between the focal mechanism solutions of these three institutions and that of the CENC are 22.79°, 9.85°, and 12.62°, respectively. Due to the influence of differences in seismic data, the selected methods, and the complexity of the velocity structure, the strike, dip, and rake show certain deviations among different earthquake agencies. The focal mechanism solution obtained by the CENC demonstrates a high degree of correspondence with those of the GFZ and the GCMT. Furthermore, it is generally consistent with the results published by the USGS.

### 4.3. Calculation of Source Parameters

4.3.1. Estimation of Source Parameters Using Seisan Explorer

To estimate earthquake spectral and source parameters, the SEISAN software was applied. The software automatically picks the spectral parameters after defining all the phase components, along with defining the maximum amplitude either in the S-wave phase or P-wave phase. The spectral parameters are: (i) low-frequency displacement spectral level (Ω0), (ii) corner frequency (fc), (iii) the frequency (fmax), and (iv) the rate of decay above fmax (N). For the calculation of the seismic moment (Mo) value, Brune's source model has been used [40,41].

The values of the source parameters are estimated using the following equations:

Seismic Moment ($M_0$) for the S seismic waves (Brune, 1970, 1971):

$$\mathrm{Mo} = \frac{4\pi\rho\beta^3 R\Omega_0}{R_{\theta\varphi} S_\alpha}$$

Where $\rho$ is the average density (=2.9 g/cm3), $\beta$ is shear wave velocity in the source zone (=3.9 km/s), $R$ is the hypocentral distance, Rθφ is the average radiation pattern (=0.63), Sα is free surface amplification (=2).

$$\mathrm{Mo} = \frac{4\pi \times (2.9 \times 1000) \times (1000 \times 3.9^3) \times 372000\, \Omega_0}{0.63 \times 2}$$

Using the value of

$$\Omega_0 = 5.75\, nm/sec$$

This low-frequency displacement spectral level ($\Omega_0$) is in log amplitude, which needs an antilog value, and the **antilog** of 5.755 (base 10) is:

$$\mathrm{antilog}_{10}(5.75) = 10^{5.75}$$

$$\Omega_0 = 10^{5.75}$$

Then,

$$\mathrm{Mo} = \frac{4\pi \times (2.9 \times 1000) \times (1000 \times 3.9^3) \times 372000 \times 10^{5.75}}{0.60 \times 2}$$

$$\mathrm{Mo} = 3.76846E + 20$$

Moment Magnitude (Mw):

$$\mathrm{Mw} = \frac{2}{3}\log(3.76846E + 20) - 6.06$$

$$\mathrm{Mw} = 7.657442251$$

From this calculation, the moment magnitude (Mw) is 7.65 (~7.7).

**Table 2.** Focal mechanism of the 2025 Myanmar earthquake from different international correspond to Figure 3d

| Nodal Plane I Strike/Dip/Rake (°) | Nodal Plane II Strike/Dip/Rake (°) | Depth (km) | Mw | Agency | Kagan Angle Relative to CENC (°) |
|---|---|---|---|---|---|
| 268/82/-32 | 3/58/-170 | 11 | 7.8 | CENC | – |
| 1/82/-174 | 270/84/-8 | 40.5 | 7.7 | USGS | 22.79 |
| 356/52/-179 | 266/89/-37 | 25 | 7.7 | GFZ | 9.85 |
| 353/60/175 | 85/86/30 | 19 | 7.7 | GCMT | 12.62 |

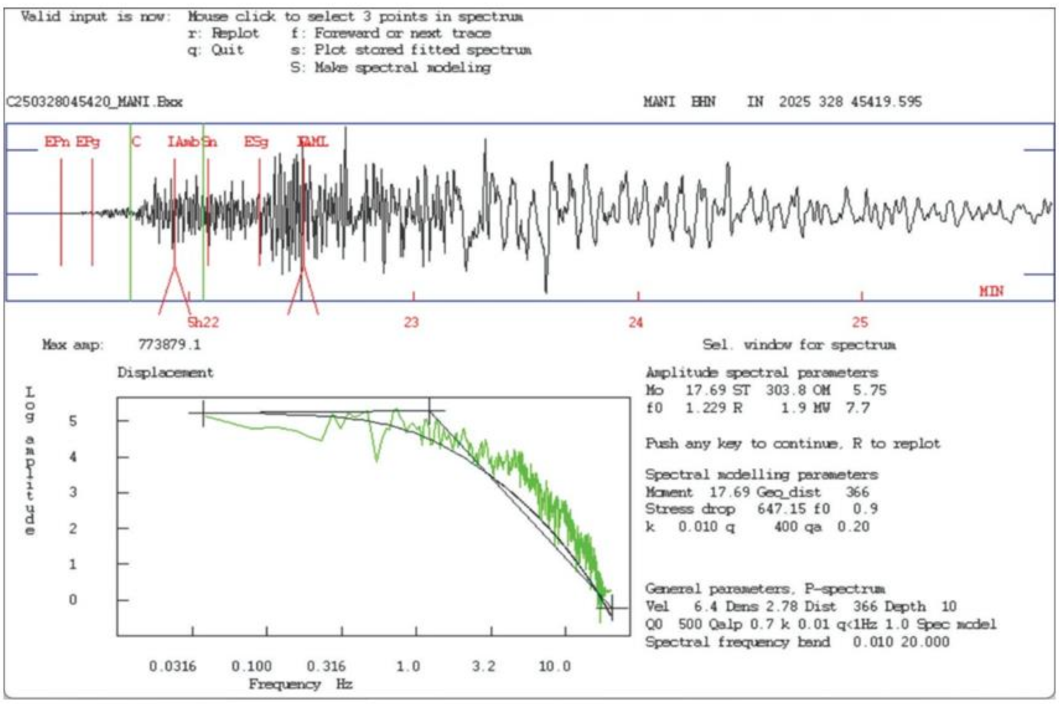


**Figure 4.** Fourier transform spectrum used for moment magnitude estimation

**Table 3.** Table showing earthquake source parameters, including epicenter, focal depth, and magnitude

| Locate | Save | Prev event | Next event |
|---|---|---|---|

| Date | Time | +/- 0.42 s | Distance Indicator | Event Indicator |
|---|---|---|---|---|
| 2025-03-28 | 06:20:52.0 | | R | |

| Latitude | +/- 7.4 km | Longitude | +/- 12 km | Depth | +/- 0 km |
|---|---|---|---|---|---|
| 22.0130 | | 95.9350 | | 10.00 | |

| Locality | Depth flag | Epi flag |
|---|---|---|
| | | |

| RMS: 0.20 | Dx: -0.0 | Dy: -0.0 | Dz: 0.0 | Dot: 0.0 | Gap: 360 | NSt: 1 |
|---|---|---|---|---|---|---|

| Mangitudes | | Settings |
|---|---|---|
| Value | Type | Agency |
| 7.4 | L | MAN |
| 5.3 | C | MAN |
| 7.7 | W | MAN |

| Phase | Azimuth | | Mangitude | | Log | | | | | | | | | | | | | |
|---|---|---|---|---|---|---|---|---|---|---|---|---|---|---|---|---|---|---|
| # | Station | Component | Nt | Lo | Date/Time (UTC) | Distance (km) | Azimuth (°) | Onset | Phase Obs | T-Obs (s) | Phase Cal | Wt Obs | PhCal | Ain | WtCal | T-Cal | Res | Imp |
| 1 | MANI | B E | | | 2025-03-28 06:21:45.42 | 366 | 326 | E | Pn | 53.42 | PN4 | | | 48 | 1 | 53.32 | 0.1 | 1 |
| 2 | MANI | B N | | | 2025-03-28 06:21:45.42 | 366 | 326 | E | Pn | 53.42 | PN4 | | | 48 | 1 | 53.32 | 0.1 | 1 |
| 3 | MANI | B Z | | | 2025-03-28 06:21:45.43 | 366 | 326 | E | Pn | 53.43 | PN4 | | | 48 | 1 | 53.32 | 0.11 | 1 |
| 4 | MANI | B Z | | | 2025-03-28 06:21:51.25 | 366 | 326 | E | | | | | | | | | | |
| 5 | MANI | B Z | | | 2025-03-28 06:21:53.63 | 366 | 326 | E | Pg | 61.63 | PG | | | 91 | 1 | 61.39 | 0.24 | 3 |
| 6 | MANI | B N | | | 2025-03-28 06:21:53.64 | 366 | 326 | E | Pg | 61.64 | PG | | | 91 | 1 | 61.39 | 0.25 | 3 |
| 7 | MANI | B E | | | 2025-03-28 06:21:53.65 | 366 | 326 | E | Pg | 61.65 | PG | | | 91 | 1 | 61.39 | 0.26 | 3 |
| 8 | MANI | B Z | | | 2025-03-28 06:22:24.55 | 366 | 326 | | Sn | 92.55 | SN4 | | | 48 | 1 | 92.78 | -0.23 | 4 |
| 9 | MANI | B N | | | 2025-03-28 06:22:24.76 | 366 | 326 | | Sn | 92.76 | SN4 | | | 48 | 1 | 92.78 | -0.02 | 4 |
| 10 | MANI | B E | | | 2025-03-28 06:22:24.86 | 366 | 326 | | Sn | 92.86 | SN4 | | | 48 | 1 | 92.78 | 0.08 | 4 |
| 11 | MANI | B N | | | 2025-03-28 06:22:38.58 | 366 | 326 | E | Sg | 106.58 | SG | | | 91 | 1 | 106.82 | -0.24 | 8 |
| 12 | MANI | B Z | | | 2025-03-28 06:22:38.68 | 366 | 326 | E | Sg | 106.68 | SG | | | 91 | 1 | 106.82 | -0.14 | 8 |

## 5. Discussion

The focal mechanism solution of the 28 March 2025 Myanmar earthquake clearly indicates a dextral strike-slip event, with the fault plane trending approximately N–S, parallel to the trace of the Sagaing Fault, and a focal depth of about 10 km. The Sagaing Fault is one of the most active and seismically hazardous structures in the region, accommodating a significant proportion of the stress generated by the ongoing oblique convergence between the Indian Plate and the Myanmar Microplate. Its role as a major lithospheric boundary means that large-magnitude earthquakes along this fault are directly linked to the long-term accumulation of tectonic strain.

Field observations following the earthquake (Figs. 5 and 6) reveal extensive surface rupture, with measurable right-lateral offsets ranging from approximately 2 m to 6 m. Such high displacement values are consistent with the dominant shear motion expected from a dextral strike-slip fault, particularly along the high-strain central and southern segments of the Sagaing Fault. These field measurements correlate well with the seismological solution, which confirms the fault's right-lateral movement as the principal mode of slip during the event.

The orientation of the three principal stresses from the focal mechanism indicates that $\sigma_2$ exhibits the maximum plunge, a configuration characteristic of strike-slip-dominated faulting. However, the solution also shows a minor normal-faulting component, likely the result of a slight inclination of $\sigma_1$ relative to the plunge of $\sigma_3$. This secondary extensional component may explain the occurrence of surface cracks and ground opening documented in the field and in video footage recorded just days after the mainshock (Fig. 7). These features suggest that local stress perturbations during rupture can lead to complex near-surface deformation patterns, particularly in zones of geometric irregularity along the fault trace.


**Figure 5.** Offset of the Mandalay-Shwebo Highway (imagery sourced from https://soar.earth/). a Pre-earthquake imagery; b Post-earthquake imagery; c Photograph of the Mandalay-Shwebo Highway (Source: Twitter account @heungburma)


**Figure 6.** Field photographs of the coseismic slips of the earthquake surface rupture zone along the SSF (Source: Twitter account @heungburma). a–d represent coseismic slips measured from offset roads at four different sites


**Figure 7.** Large cracks and openings on the ground leading to sudden subsidence and collapse of buildings

From a broader tectonic perspective, the occurrence of such a large earthquake on the Sagaing Fault is linked to the regional partitioning of India–Sunda plate motion across the Indo–Burma Arc (IBA). GPS geodetic data show that India–Sunda relative motion, measured at ~37 mm/yr and oriented N11 °E, is distributed among three principal structures: the blind megathrust (~7 mm/yr), the Churachandpur–Mao Fault (~17 mm/yr), and the Sagaing Fault (~18 ± 2 mm/yr). This distribution of slip rates indicates that the Sagaing Fault accommodates nearly half of the total relative motion between the plates in this part of the arc.

Slip on the Sagaing Fault is predominantly accommodated through stick–slip behaviour, consistent with the sudden release of accumulated strain during large earthquakes [28,42,21]. Nevertheless, geodetic and field studies have also reported fault creep along its northern segment [28,42]. This creeping behaviour poses an apparent paradox, as it would be expected to inhibit the occurrence of large seismic events. However, the historical record demonstrates otherwise, with significant earthquakes such as the 1931 M7.6 event occurring in this zone. This suggests a spatially variable locking behaviour along the fault, where creeping sections may be interspersed with locked patches capable of generating large earthquakes.

The 2025 event thus highlights the Sagaing Fault's dual nature as both a creeping and seismically active fault, and underscores the importance of understanding the interplay between interseismic creep, fault locking, and rupture propagation in assessing the seismic hazard of the Indo–Burma region.

### 5.1. Energy Release

Energy release during an earthquake can also be expressed in another type of magnitude called Energy Magnitude (Me). However, Energy Magnitude and Moment Magnitude (Mw) do not have identical values since two different properties of an earthquake are used to decipher these magnitudes.

Therefore, a simple relation of Energy Release can be obtained using the equation given below.

$\mathrm{Log}_{10}E = 5.24 + 1.44$ Mw, expressed in joules

For our Myanmar Earthquake, the moment magnitude is 7.7 Mw.

Then, by using the value of Mw = 7.7 in the above equation, we have

$\mathrm{Log}_{10}E = 5.24 + 1.44 \times 7.7$
$\mathrm{Log}_{10}E = 5.24 + 11.088$
$= 16.328$

After applying antilog to the value of the energy (E), in joules, we get

$E = 10^{16.328} \approx 2.13 \times 10^{16}$ J

So, the Myanmar earthquake of March 28, 2025, released about $2.13 \times 10^{16}$ joules of energy.

$2.13 \times 10^{16}$ joules ≈ 5.09 megatons of TNT

Fun fact: The Hiroshima atomic bomb, dropped on August 6, 1945, released about $6.3 \times 10^{13}$ joules of energy. By comparison, the 7.7 Myanmar earthquake unleashed around 338 times the energy released by the Hiroshima Atom Bomb at once.

## 6. Conclusions

This paper presents a preliminary analysis of the Mw 7.7 earthquake that struck Myanmar in 2025. The earthquake occurred along the Sagaing Fault Zone. The focal mechanism solution reveals that this earthquake is associated with a strike-slip fault. Analysis of the rupture process shows that the rupture is predominantly oriented in a north-south (NS) direction, demonstrating unilateral southward rupture propagation. This earthquake exerted tremendous destructive force, inflicting severe casualties and substantial property damage in Myanmar. We post the following potential contributing factors:

(1) This earthquake reached a magnitude of 7.71 Mw, releasing enormous energy. With a focal depth of just 10 km, it was a shallow-focus earthquake, resulting in minimal attenuation of seismic energy at the surface. This caused intense ground shaking and significantly increased the destructive force on buildings.

(2) Buildings in Myanmar generally have a low seismic resistance grade and cannot withstand the impacts of strong earthquakes.

(3) The epicenter was near Mandalay's urban core, a densely populated area where high population density expanded the disaster's impact, concentrating casualties and property losses. The seismic parameters, like the focal mechanism and rupture process from this study, can offer more precise data for seismic hazard assessment in these areas. Thus, relevant departments can formulate better emergency plans based on our analysis of this earthquake's damage, strengthening response capabilities and reducing losses.

(4) The stress orientation of NE-SW compression and NW-SE extension at the earthquake source of this Myanmar Earthquake causes a westerly push /pressure to the IMR, which, combined with the NE movement of the Indian plate, produces EW compression and NS extension in the IMR that deform the rocks of the region through a shear-coupled dextral strike-slip mechanism.

## Appendix

**Table 4.** Polarity data obtained from International Seismological Centre (ISC) and recalculate the angle of incidence and Azimuth from epicentral distance and azimuth

| Sl. No.: | Station Name | P-wave arrival time | Distance | Incidence Angle | Azimuth | Polarity |
|---|---|---|---|---|---|---|
| 1 | HKPS | 24:51.9 | 16.96 | 49 | 85 | d |
| 2 | MALK | 25:25.4 | 19.93 | 54 | 230 | d |
| 3 | MALK | 25:25.4 | 19.93 | 54 | 230 | d |
| 4 | PALK | 25:35.0 | 20.61 | 56 | 227 | d |
| 5 | PALK | 25:35.0 | 20.61 | 56 | 227 | d |
| 6 | MRZ1 | 26:12.9 | 24.31 | 62 | 330 | c |
| 7 | ASAI | 26:16.5 | 25.04 | 62 | 324 | c |
| 8 | TARG | 26:19.4 | 24.93 | 62 | 327 | c |
| 9 | YOJ | 26:23.5 | 25.08 | 62 | 79 | d |
| 10 | ANVS | 26:25.4 | 25.78 | 62 | 328 | c |
| 11 | BOOM | 26:30.3 | 26.45 | 62 | 326 | c |
| 12 | DRK | 26:32.7 | 26.98 | 62 | 316 | c |
| 13 | HMDM | 26:33.5 | 26.55 | 62 | 239 | d |
| 14 | HMDM | 26:33.5 | 26.55 | 62 | 239 | d |
| 15 | KBU | 26:34.1 | 26.61 | 62 | 304 | c |
| 16 | OHH | 26:34.8 | 26.96 | 62 | 319 | c |
| 17 | ARLS | 26:35.3 | 26.89 | 62 | 323 | c |
| 18 | ULN | 26:36.6 | 27.43 | 62 | 17 | d |
| 19 | ULN | 26:36.6 | 27.43 | 62 | 17 | d |
| 20 | AAK | 26:38.5 | 27.32 | 62 | 324 | c |
| 21 | MAKZ | 26:38.5 | 27.29 | 62 | 339 | c |
| 22 | FRU1 | 26:40.6 | 27.37 | 62 | 325 | c |
| 23 | BTK | 26:45.2 | 27.93 | 62 | 316 | c |
| 24 | ARK | 26:47.6 | 28.21 | 62 | 320 | c |
| 25 | TRKS | 26:49.1 | 28.51 | 62 | 319 | c |
| 26 | KAAM | 27:13.4 | 30.8 | 63 | 229 | d |
| 27 | KAAM | 27:13.4 | 30.8 | 63 | 229 | d |

| Sl. No.: | Station Name | P-wave arrival time | Distance | Incidence Angle | Azimuth | Polarity |
|---|---|---|---|---|---|---|
| 28 | KURK | 27:15.6 | 31.78 | 63 | 339 | c |
| 29 | UOSS | 27:59.5 | 36.42 | 64 | 283 | c |
| 30 | UOSS | 27:59.5 | 36.42 | 64 | 283 | c |
| 31 | RAYN | 29:20.4 | 46.28 | 66 | 282 | c |
| 32 | RAYN | 29:20.4 | 46.28 | 66 | 282 | c |
| 33 | GNI | 29:25.1 | 46.77 | 66 | 305 | c |
| 34 | HAKT | 29:29.0 | 47.32 | 66 | 301 | c |
| 35 | HAKT | 29:29.0 | 47.32 | 66 | 301 | c |
| 36 | OZAP | 29:29.5 | 47.18 | 66 | 303 | c_ |
| 37 | DIGO | 29:33.3 | 47.84 | 67 | 305 | c |
| 38 | EPOS | 29:38.4 | 48.45 | 67 | 307 | c |
| 39 | KIV | 29:39.8 | 48.81 | 67 | 310 | c |
| 40 | KIV | 29:43.2 | 48.81 | 67 | 310 | c |
| 41 | DAMY | 29:46.9 | 49.24 | 67 | 271 | c |
| 42 | DAMY | 29:46.9 | 49.24 | 67 | 271 | c |
| 43 | KELT | 29:57.6 | 50.95 | 67 | 305 | c |
| 44 | ARPR | 30:00.1 | 51.62 | 67 | 303 | c |
| 45 | KEMA | 30:00.1 | 51.5 | 67 | 303 | c |
| 46 | ROCA | 30:07.2 | 52.17 | 67 | 220 | d |
| 47 | ROCA | 30:07.2 | 52.17 | 67 | 220 | d |
| 48 | ANDN | 30:12.1 | 53.16 | 67 | 301 | c |
| 49 | ANDN | 30:12.1 | 53.16 | 67 | 301 | c |
| 50 | BALJ | 30:18.8 | 54.01 | 68 | 294 | c |
| 51 | BALJ | 30:18.8 | 54.01 | 68 | 294 | c |
| 52 | GHAJ | 30:20.1 | 54.15 | 68 | 294 | c |
| 53 | GHAJ | 30:20.1 | 54.15 | 68 | 294 | c |
| 54 | OBN | 30:22.5 | 54.84 | 68 | 323 | c |
| 55 | KLMR | 30:23.9 | 54.88 | 68 | 330 | c |
| 56 | EIL | 30:24.4 | 54.86 | 68 | 292 | c |
| 57 | EIL | 30:24.4 | 54.86 | 68 | 292 | c |
| 58 | MSBI | 30:25.0 | 54.33 | 68 | 294 | c |
| 59 | MSBI | 30:25.0 | 54.33 | 68 | 294 | c |
| 60 | ILGA | 30:26.7 | 55.2 | 68 | 306 | c |
| 61 | KIRS | 30:29.1 | 55.05 | 68 | 303 | c |
| 62 | CSS | 30:31.1 | 55.71 | 68 | 298 | c |
| 63 | CSS | 30:31.1 | 55.71 | 68 | 298 | c |
| 64 | KKUL | 30:31.5 | 55.83 | 68 | 303 | c |
| 65 | ANTO | 30:32.3 | 55.91 | 68 | 304 | c |
| 66 | ANTO | 30:35.8 | 55.91 | 68 | 304 | c |
| 67 | KEPZ | 30:42.4 | 56.97 | 68 | 301 | c |
| 68 | KEPZ | 30:42.4 | 56.97 | 68 | 301 | c |
| 69 | SAHE | 30:45.3 | 57.37 | 68 | 305 | c |
| 70 | ISP | 30:46.4 | 57.78 | 68 | 302 | c |
| 71 | KIEV | 30:48.7 | 58.64 | 69 | 317 | c |
| 72 | RER | 30:50.3 | 58.01 | 69 | 225 | d |
| 73 | RER | 30:50.3 | 58.01 | 69 | 225 | d |
| 74 | KIEV | 30:52.9 | 58.65 | 69 | 317 | c |
| 75 | TIRR | 30:53.3 | 59.08 | 69 | 310 | c |
| 76 | LVZ | 30:53.8 | 59.17 | 69 | 337 | c |
| 77 | CFR | 30:53.9 | 59.26 | 69 | 310 | c |

| Sl. No.: | Station Name | P-wave arrival time | Distance | Incidence Angle | Azimuth | Polarity |
|---|---|---|---|---|---|---|
| 78 | PUL | 30:54.0 | 59.05 | 69 | 328 | c |
| 79 | TLCR | 30:54.7 | 58.78 | 69 | 310 | c |
| 80 | KLYT | 30:54.7 | 58.72 | 69 | 306 | c |
| 81 | SORM | 30:56.4 | 59.12 | 69 | 314 | c |
| 82 | TIRR | 30:57.1 | 59.08 | 69 | 310 | c |
| 83 | CFR | 30:58.2 | 59.26 | 69 | 310 | c |
| 84 | CTYL | 30:58.7 | 59.27 | 69 | 306 | c |
| 85 | BALY | 30:59.4 | 59.9 | 69 | 304 | c |
| 86 | SCTR | 30:59.6 | 59.35 | 69 | 311 | c |
| 87 | ICOR | 30:59.7 | 59.52 | 69 | 309 | c |
| 88 | TUDR | 31:00.1 | 59.58 | 69 | 311 | c |
| 89 | BAND | 31:00.2 | 59.48 | 69 | 305 | c |
| 90 | RO04 | 31:01.4 | 59.75 | 69 | 310 | c |
| 91 | KU6 | 31:01.7 | 60.47 | 69 | 335 | c |
| 92 | VRI | 31:02.1 | 60.24 | 69 | 311 | c |
| 93 | TESR | 31:02.1 | 60.28 | 69 | 312 | c |
| 94 | PANC | 31:02.7 | 59.94 | 69 | 311 | c |
| 95 | ISR | 31:03.0 | 60.39 | 69 | 310 | c |
| 96 | BG05 | 31:03.5 | 60.03 | 69 | 308 | c |
| 97 | RO27 | 31:03.6 | 59.96 | 69 | 312 | c |
| 98 | BG01 | 31:03.9 | 59.98 | 69 | 309 | c |
| 99 | VSU | 31:04.5 | 60.7 | 69 | 326 | c |
| 100 | MSF | 31:04.9 | 60.78 | 69 | 334 | c |
| 101 | TESR | 31:05.1 | 60.28 | 69 | 312 | c |
| 102 | VRI | 31:05.4 | 60.24 | 69 | 311 | c |
| 103 | NARR | 31:05.6 | 60.23 | 69 | 311 | c |
| 104 | BDRM | 31:05.7 | 60.28 | 69 | 301 | c |
| 105 | BG12 | 31:05.9 | 60.36 | 69 | 307 | c |
| 106 | MLR | 31:06.1 | 60.8 | 69 | 311 | c |
| 107 | LOZB | 31:06.5 | 60.43 | 69 | 308 | c |
| 108 | PRAR | 31:06.8 | 60.55 | 69 | 313 | c |
| 109 | BG04 | 31:08.0 | 60.56 | 69 | 308 | c |
| 110 | KSV | 31:08.7 | 61.31 | 69 | 314 | c |
| 111 | MLR | 31:09.0 | 60.8 | 69 | 311 | c |
| 112 | VOIR | 31:09.6 | 61.43 | 69 | 311 | c |
| 113 | ZKR | 31:09.9 | 61.5 | 69 | 299 | c |
| 114 | ZKR | 31:09.9 | 61.5 | 69 | 299 | c |
| 115 | ELND | 31:10.5 | 60.98 | 69 | 308 | c |
| 116 | RDO | 31:10.6 | 61.37 | 69 | 306 | c |
| 117 | RO12 | 31:11.2 | 61.08 | 69 | 310 | c |
| 118 | ARR | 31:11.6 | 61.73 | 69 | 311 | c |
| 119 | DOPR | 31:12.1 | 61.17 | 69 | 311 | c |
| 120 | APE | 31:12.2 | 61.8 | 69 | 301 | c |
| 121 | THER | 31:12.7 | 61.93 | 69 | 301 | c |
| 122 | PABE | 31:13.1 | 62.02 | 69 | 322 | c |
| 123 | MTSE | 31:13.3 | 62.25 | 69 | 326 | c |
| 124 | ARCR | 31:13.5 | 61.84 | 69 | 313 | c |
| 125 | OUL | 31:13.7 | 61.93 | 69 | 333 | c |
| 126 | KMBO | 31:13.8 | 61.54 | 69 | 256 | d |
| 127 | KMBO | 31:13.8 | 61.54 | 69 | 256 | d |

| Sl. No.: | Station Name | P-wave arrival time | Distance | Incidence Angle | Azimuth | Polarity |
|---|---|---|---|---|---|---|
| 128 | SGF | 31:14.6 | 62.06 | 69 | 336 | c |
| 129 | MEF | 31:15.0 | 62.05 | 69 | 328 | c |
| 130 | RO37 | 31:15.8 | 61.75 | 69 | 313 | c |
| 131 | CRAR | 31:15.9 | 62.39 | 70 | 310 | c |
| 132 | SUW | 31:16.4 | 62.45 | 70 | 321 | c |
| 133 | BMR | 31:16.6 | 62.39 | 70 | 313 | c |
| 134 | TNR | 31:16.9 | 61.96 | 69 | 311 | c |
| 135 | KEV | 31:17.0 | 62.34 | 70 | 339 | c |
| 136 | KEV | 31:17.1 | 62.34 | 70 | 339 | c |
| 137 | OUF | 31:17.5 | 62.32 | 70 | 332 | c |
| 138 | KWP | 31:18.9 | 62.83 | 70 | 316 | c |
| 139 | RO32 | 31:19.0 | 62.19 | 69 | 313 | c |
| 140 | ABPO | 31:19.6 | 62.56 | 70 | 233 | d |
| 141 | ABPO | 31:19.6 | 62.56 | 70 | 233 | d |
| 142 | DEV | 31:20.0 | 62.91 | 70 | 311 | c |
| 143 | BMR | 31:20.0 | 62.39 | 70 | 313 | c |
| 144 | SLIT | 31:20.2 | 63.01 | 70 | 325 | c |
| 145 | CJR | 31:20.3 | 62.37 | 70 | 312 | c |
| 146 | DRGR | 31:20.4 | 62.98 | 70 | 312 | c |
| 147 | VTS | 31:20.5 | 62.94 | 70 | 308 | c |
| 148 | RO18 | 31:21.6 | 62.7 | 70 | 311 | c |
| 149 | PBUR | 31:22.0 | 63.18 | 70 | 323 | c |
| 150 | TRPA | 31:22.0 | 63.01 | 70 | 314 | c |
| 151 | PTSR | 31:22.1 | 62.86 | 70 | 311 | c |
| 152 | HEF | 31:22.2 | 63.29 | 70 | 337 | c |
| 153 | MESR | 31:22.3 | 62.79 | 70 | 313 | c |
| 154 | DEV | 31:22.7 | 62.91 | 70 | 311 | c |
| 155 | RAF | 31:23.5 | 63.4 | 70 | 328 | c |
| 156 | VTS | 31:23.7 | 62.94 | 70 | 308 | c |
| 157 | BZS | 31:25.7 | 63.81 | 70 | 311 | c |
| 158 | HERR | 31:26.3 | 63.33 | 70 | 310 | c |
| 159 | RO20 | 31:27.4 | 63.51 | 70 | 311 | c |
| 160 | KTHA | 31:27.4 | 63.87 | 70 | 301 | c |
| 161 | BORR | 31:27.8 | 63.59 | 70 | 313 | c |
| 162 | BEL | 31:28.3 | 63.94 | 70 | 318 | c |
| 163 | MFRD | 31:28.6 | 63.74 | 70 | 312 | c |
| 164 | MDVR | 31:29.0 | 63.83 | 70 | 310 | c |
| 165 | BZS | 31:29.1 | 63.83 | 70 | 311 | c |
| 166 | RO10 | 31:29.2 | 63.75 | 70 | 311 | c |
| 167 | KIF | 31:29.6 | 64.4 | 70 | 337 | c |
| 168 | BOVS | 31:30.1 | 63.95 | 70 | 309 | c |
| 169 | NIE | 31:30.6 | 64.39 | 70 | 316 | c |
| 170 | ITM | 31:30.9 | 64.63 | 70 | 302 | c |
| 171 | BSZH | 31:31.4 | 64.6 | 70 | 313 | c |
| 172 | OJC | 31:31.7 | 64.67 | 70 | 316 | c |
| 173 | AMBH | 31:32.2 | 64.38 | 70 | 312 | c |
| 174 | VOI | 31:32.8 | 64.68 | 70 | 231 | d |
| 175 | VOI | 31:32.8 | 64.68 | 70 | 231 | d |
| 176 | PSZ | 31:33.5 | 64.8 | 70 | 314 | c |
| 177 | BSZH | 31:34.5 | 64.6 | 70 | 313 | c |

| Sl. No.: | Station Name | P-wave arrival time | Distance | Incidence Angle | Azimuth | Polarity |
|---|---|---|---|---|---|---|
| 178 | SJES | 31:35.4 | 65.42 | 70 | 309 | c |
| 179 | PSZ | 31:35.9 | 64.8 | 70 | 314 | c |
| 180 | BUD | 31:36.2 | 65.43 | 70 | 313 | c |
| 181 | MORH | 31:38.0 | 65.83 | 70 | 312 | c |
| 182 | PDG | 31:38.2 | 65.88 | 70 | 308 | c |
| 183 | OKC | 31:38.3 | 65.76 | 70 | 316 | c |
| 184 | MAUC | 31:40.0 | 66.02 | 70 | 316 | c |
| 185 | GKP | 31:40.3 | 66.02 | 70 | 320 | c |
| 186 | MORC | 31:40.9 | 66.16 | 70 | 316 | c |
| 187 | KOVH | 31:41.7 | 66.22 | 70 | 312 | c |
| 188 | PDG | 31:42.4 | 65.89 | 70 | 308 | c |
| 189 | HSPB | 31:43.0 | 66.65 | 71 | 346 | c |
| 190 | TIH | 31:43.3 | 66.26 | 70 | 313 | c |
| 191 | MPLH | 31:43.5 | 66.47 | 70 | 313 | c |
| 192 | KRLC | 31:44.3 | 66.61 | 70 | 316 | c |
| 193 | EGYH | 31:44.6 | 66.57 | 70 | 314 | c |
| 194 | MORC | 31:45.0 | 66.16 | 70 | 316 | c |
| 195 | KSP | 31:46.2 | 66.84 | 71 | 317 | c |
| 196 | BLY | 31:46.5 | 67.04 | 71 | 311 | c |
| 197 | SOP | 31:47.0 | 67.06 | 71 | 314 | c |
| 198 | DPC | 31:47.7 | 66.88 | 71 | 317 | c |
| 199 | BSD | 31:47.9 | 67.2 | 71 | 322 | c |
| 200 | VRAC | 31:48.4 | 66.83 | 71 | 316 | c |
| 201 | UPC | 31:48.4 | 67.05 | 71 | 317 | c |
| 202 | KBS | 31:49.1 | 67.5 | 71 | 348 | c |
| 203 | BLY | 31:50.6 | 67.04 | 71 | 311 | c |
| 204 | TREC | 31:50.8 | 67.55 | 71 | 316 | c |
| 205 | STAC | 31:51.2 | 67.7 | 71 | 315 | c |
| 206 | ARSA | 31:51.6 | 67.81 | 71 | 314 | c |
| 207 | PRU | 31:52.8 | 68.06 | 71 | 317 | c |
| 208 | MATE | 31:52.9 | 68.06 | 71 | 306 | c |
| 209 | PVCC | 31:52.9 | 67.97 | 71 | 317 | c |
| 210 | RUE | 31:54.4 | 68.19 | 71 | 319 | c |
| 211 | RGN | 31:55.0 | 68.19 | 71 | 322 | c |
| 212 | ZVC | 31:55.4 | 68.36 | 71 | 316 | c |
| 213 | BRG | 31:55.8 | 68.31 | 71 | 318 | c |
| 214 | MATE | 31:55.9 | 68.06 | 71 | 306 | c |
| 215 | MOA | 31:56.3 | 68.56 | 71 | 314 | c |
| 216 | HSKC | 31:56.7 | 68.67 | 71 | 317 | c |
| 217 | GEC2 | 31:57.2 | 68.77 | 71 | 315 | c |
| 218 | OBKA | 31:57.4 | 68.59 | 71 | 313 | c |
| 219 | STKA | 31:57.6 | 69.11 | 71 | 139 | c |
| 220 | GEC7 | 31:57.6 | 68.77 | 71 | 315 | c |
| 221 | MARC | 31:57.8 | 68.8 | 71 | 306 | c |
| 222 | CUC | 31:57.9 | 68.86 | 71 | 306 | c |
| 223 | CLL | 31:58.2 | 68.83 | 71 | 318 | c |
| 224 | LLD | 31:58.3 | 68.72 | 71 | 322 | c |
| 225 | DRE | 31:59.3 | 69.27 | 71 | 313 | c |
| 226 | KHC | 31:59.5 | 68.81 | 71 | 316 | c |
| 227 | WET | 32:00.4 | 69.26 | 71 | 316 | c |

| Sl. No.: | Station Name | P-wave arrival time | Distance | Incidence Angle | Azimuth | Polarity |
|---|---|---|---|---|---|---|
| 228 | TANN | 32:00.5 | 69.31 | 71 | 317 | c |
| 229 | PRED | 32:00.6 | 69.27 | 71 | 313 | c |
| 230 | ACOM | 32:00.8 | 69.29 | 71 | 313 | c |
| 231 | SABO | 32:00.9 | 69.31 | 71 | 312 | c |
| 232 | KBA | 32:01.6 | 69.31 | 71 | 314 | c |
| 233 | NEUB | 32:02.8 | 69.61 | 71 | 318 | c |
| 234 | KONO | 32:03.0 | 69.51 | 71 | 327 | c |
| 235 | OVD | 32:03.5 | 69.54 | 71 | 325 | c |
| 236 | FLT1 | 32:04.2 | 69.75 | 71 | 319 | c |
| 237 | ZARR | 32:04.2 | 69.73 | 71 | 321 | c |
| 238 | FALK | 32:04.4 | 69.84 | 71 | 319 | c |
| 239 | MOX | 32:04.4 | 69.81 | 71 | 318 | c |
| 240 | CIMO | 32:05.1 | 70.06 | 71 | 313 | c |
| 241 | GRB3 | 32:05.6 | 69.92 | 71 | 316 | c |
| 242 | GRB1 | 32:05.9 | 70.01 | 71 | 316 | c |
| 243 | BSEG | 32:06.1 | 70.02 | 71 | 321 | c |
| 244 | AQU | 32:06.4 | 70.17 | 71 | 309 | c |
| 245 | GRC1 | 32:06.6 | 70.17 | 71 | 316 | c |
| 246 | GRB5 | 32:06.7 | 70.04 | 71 | 316 | c |
| 247 | GRB4 | 32:06.8 | 70.05 | 71 | 316 | c |
| 248 | GRA3 | 32:06.9 | 70.15 | 71 | 317 | c |
| 249 | GRA2 | 32:06.9 | 70.15 | 71 | 317 | c |
| 250 | GRC2 | 32:07.0 | 70.28 | 71 | 316 | c |
| 251 | GRA1 | 32:07.5 | 70.23 | 71 | 317 | c |
| 252 | MUD | 32:07.6 | 70.23 | 71 | 324 | c |
| 253 | FUR | 32:07.7 | 70.48 | 71 | 315 | c |
| 254 | CLZ | 32:08.0 | 70.36 | 71 | 319 | c |
| 255 | GRFO | 32:08.6 | 70.23 | 71 | 317 | c |
| 256 | GTTG | 32:10.0 | 70.67 | 71 | 319 | c |
| 257 | UBBA | 32:10.3 | 70.78 | 71 | 318 | c |
| 258 | GOLD | 32:10.4 | 70.73 | 71 | 320 | c |
| 259 | RETH | 32:12.8 | 70.8 | 71 | 320 | c |
| 260 | LUEB | 32:13.5 | 71.29 | 72 | 320 | c |
| 261 | DAVA | 32:15.3 | 71.58 | 72 | 314 | c |
| 262 | UBR | 32:15.5 | 71.35 | 72 | 315 | c |
| 263 | STU | 32:16.0 | 71.71 | 72 | 316 | c |
| 264 | IBBN | 32:16.6 | 71.85 | 72 | 320 | c |
| 265 | KAST | 32:17.5 | 71.68 | 72 | 319 | c |
| 266 | TNS | 32:17.8 | 71.87 | 72 | 318 | c |
| 267 | SLE | 32:18.9 | 72.39 | 72 | 315 | c |
| 268 | MUGI | 32:19.3 | 72.45 | 72 | 313 | c |
| 269 | BFO | 32:19.8 | 72.37 | 72 | 316 | c |
| 270 | WTSB | 32:20.1 | 72.5 | 72 | 320 | c |
| 271 | BUG | 32:20.5 | 72.33 | 72 | 319 | c |
| 272 | BNAL | 32:21.5 | 72.65 | 72 | 314 | c |
| 273 | ECH | 32:24.3 | 73.16 | 72 | 316 | c |
| 274 | PGF | 32:25.2 | 73.3 | 72 | 310 | c |
| 275 | HGN | 32:25.3 | 73.31 | 72 | 319 | c |
| 276 | BOUR | 32:25.6 | 73.31 | 72 | 315 | c |
| 277 | SMPL | 32:25.8 | 73.21 | 72 | 309 | c |

| Sl. No.: | Station Name | P-wave arrival time | Distance | Incidence Angle | Azimuth | Polarity |
|---|---|---|---|---|---|---|
| 278 | MEM | 32:26.5 | 73.3 | 72 | 318 | c |
| 279 | WLF | 32:26.9 | 73.45 | 72 | 317 | c |
| 280 | RCHB | 32:28.9 | 73.9 | 72 | 318 | c |
| 281 | SAOF | 32:29.0 | 73.95 | 72 | 311 | c |
| 282 | DAG | 32:29.9 | 74.22 | 72 | 347 | c |
| 283 | ESCA | 32:30.0 | 74.12 | 72 | 311 | c |
| 284 | UCC | 32:31.0 | 74.27 | 72 | 319 | c |
| 285 | ISO | 32:31.2 | 74.25 | 72 | 312 | c |
| 286 | GIME | 32:31.8 | 74.17 | 72 | 314 | c |
| 287 | OGAG | 32:33.5 | 74.44 | 72 | 312 | c |
| 288 | OGDI | 32:34.4 | 74.84 | 72 | 312 | c |
| 289 | ORIF | 32:34.9 | 74.86 | 72 | 313 | c |
| 290 | LOR | 32:38.2 | 75.56 | 73 | 315 | c |
| 291 | RUSF | 32:38.8 | 75.42 | 73 | 312 | c |
| 292 | ARBF | 32:39.5 | 75.64 | 73 | 311 | c |
| 293 | SSB | 32:40.9 | 75.67 | 73 | 313 | c |
| 294 | LSZ | 32:41.8 | 75.9 | 73 | 247 | d |
| 295 | LSZ | 32:41.8 | 75.9 | 73 | 247 | d |
| 296 | WACR | 32:42.7 | 75.95 | 73 | 321 | c |
| 297 | DRUM | 32:44.1 | 76.35 | 73 | 326 | c |
| 298 | EDMD | 32:46.2 | 76.75 | 73 | 324 | c |
| 299 | BIGH | 32:46.6 | 76.54 | 73 | 328 | c |
| 300 | MAHO | 32:50.3 | 77.47 | 73 | 308 | c |
| 301 | ESK | 32:50.4 | 77.26 | 73 | 325 | c |
| 302 | MTLF | 32:51.9 | 77.85 | 73 | 312 | c |
| 303 | STNC | 32:52.2 | 77.46 | 73 | 322 | c |
| 304 | MFF | 32:55.8 | 78.37 | 73 | 316 | c |
| 305 | IOMK | 32:55.8 | 78.37 | 73 | 324 | c |
| 306 | CRZF | 32:57.8 | 78.79 | 73 | 209 | d |
| 307 | CRZF | 32:57.8 | 78.79 | 73 | 209 | d |
| 308 | WLF1 | 32:58.0 | 78.63 | 73 | 323 | c |
| 309 | POGA | 32:59.3 | 79 | 73 | 235 | d |
| 310 | POGA | 32:59.3 | 79 | 73 | 235 | d |
| 311 | HTL | 33:02.0 | 79.52 | 74 | 321 | c |
| 312 | ROSF | 33:03.1 | 79.76 | 74 | 318 | c |
| 313 | IDGL | 33:03.4 | 79.64 | 74 | 325 | c |
| 314 | ATE | 33:03.6 | 79.94 | 74 | 312 | c |
| 315 | EIBI | 33:04.2 | 79.89 | 74 | 308 | c |
| 316 | ILTH | 33:04.5 | 79.42 | 73 | 324 | c |
| 317 | IWEX | 33:06.7 | 80.31 | 74 | 323 | c |
| 318 | EMOS | 33:08.3 | 80.74 | 74 | 310 | c |
| 319 | ELAN | 33:13.5 | 81.75 | 74 | 313 | c |
| 320 | EMUR | 33:15.8 | 82.2 | 74 | 308 | c |
| 321 | TAM | 33:16.2 | 82.07 | 74 | 291 | c |
| 322 | TAM | 33:16.2 | 82.07 | 74 | 291 | c |
| 323 | VAL | 33:17.7 | 82.43 | 74 | 323 | c |
| 324 | UCM | 33:18.3 | 82.73 | 74 | 310 | c |
| 325 | LBTB | 33:18.5 | 82.6 | 74 | 239 | d |
| 326 | LBTB | 33:18.5 | 82.6 | 74 | 239 | d |
| 327 | PAB | 33:24.7 | 83.81 | 75 | 310 | c |

| Sl. No.: | Station Name | P-wave arrival time | Distance | Incidence Angle | Azimuth | Polarity |
|---|---|---|---|---|---|---|
| 328 | SAAT | 33:27.8 | 84.79 | 75 | 350 | c |
| 329 | ECAL | 33:27.9 | 84.5 | 75 | 313 | c |
| 330 | BOSA | 33:27.9 | 84.57 | 75 | 236 | d |
| 331 | BOSA | 33:27.9 | 84.57 | 75 | 236 | d |
| 332 | EDA | 33:28.8 | 84.62 | 75 | 272 | c |
| 333 | EDA | 33:28.8 | 84.62 | 75 | 272 | c |
| 334 | EMAL | 33:29.4 | 84.97 | 75 | 308 | c |
| 335 | NIAQ | 33:30.4 | 85.13 | 75 | 350 | c |
| 336 | EMAZ | 33:33.6 | 85.58 | 75 | 315 | c |
| 337 | MTE | 33:34.2 | 85.7 | 75 | 312 | c |
| 338 | GDH | 33:36.4 | 95.44 | 76 | 272 | c |
| 339 | GDH | 33:36.4 | 95.44 | 76 | 272 | c |
| 340 | EVO | 33:38.6 | 86.83 | 75 | 310 | c |
| 341 | TSUM | 33:39.8 | 86.72 | 75 | 248 | d |
| 342 | TSUM | 33:39.8 | 86.72 | 75 | 248 | d |
| 343 | AVE | 33:47.0 | 88.62 | 76 | 305 | c |
| 344 | WIN | 33:48.2 | 88.52 | 76 | 245 | d |
| 345 | WIN | 33:48.2 | 88.52 | 76 | 245 | d |
| 346 | TIO | 33:52.4 | 89.52 | 76 | 303 | c |
| 347 | SUR | 33:53.8 | 89.7 | 76 | 235 | d |
| 348 | SUR | 33:53.8 | 89.7 | 76 | 235 | d |
| 349 | IVI | 34:04.9 | 92.27 | 76 | 344 | c |
| 350 | MAW | 34:05.3 | 92.51 | 76 | 192 | d |
| 351 | MAW | 34:05.3 | 92.51 | 76 | 192 | d |
| 352 | DBIC | 34:29.5 | 97.39 | 76 | 280 | c |
| 353 | DBIC | 34:29.5 | 97.39 | 76 | 280 | c |
| 354 | JZAX | 38:17.8 | 30.16 | 63 | 314 | c |
| 355 | NVS | 38:54.0 | 34.41 | 63 | 347 | c |
| 356 | SVE | 40:10.5 | 43.56 | 65 | 333 | c |
| 357 | GNI | 40:38.8 | 46.92 | 66 | 305 | c |
| 358 | ZEI | 40:44.5 | 47.92 | 67 | 309 | c |
| 359 | NRIK | 40:45.0 | 47.88 | 67 | 356 | c |
| 360 | KBZ | 40:52.1 | 48.79 | 67 | 310 | c |
| 361 | KIV | 40:52.4 | 48.98 | 67 | 310 | c |
| 362 | HOMI | 40:54.1 | 49.07 | 67 | 305 | c |
| 363 | NEUR | 40:54.4 | 48.86 | 67 | 309 | c |
| 364 | KIRV | 40:57.7 | 49.56 | 67 | 330 | c |
| 365 | PETR | 41:48.5 | 60.05 | 69 | 311 | c |
| 366 | SAHE | 41:55.5 | 57.52 | 68 | 305 | c |
| 367 | AKBB | 42:03.7 | 58.81 | 69 | 317 | c |
| 368 | KIEV | 42:03.7 | 58.82 | 69 | 317 | c |
| 369 | TLCR | 42:05.1 | 58.94 | 69 | 311 | c |
| 370 | TPGR | 42:07.9 | 59.23 | 69 | 310 | c |
| 371 | TATR | 42:09.2 | 59.48 | 69 | 311 | c |
| 372 | LVZ | 42:10.4 | 59.35 | 69 | 337 | c |
| 373 | RO27 | 42:13.5 | 60.12 | 69 | 312 | c |
| 374 | BG05 | 42:14.6 | 60.18 | 69 | 308 | c |
| 375 | VRI | 42:15.1 | 60.4 | 69 | 311 | c |
| 376 | NARR | 42:16.3 | 60.4 | 69 | 311 | c |
| 377 | TESR | 42:16.4 | 60.44 | 69 | 312 | c |

| Sl. No.: | Station Name | P-wave arrival time | Distance | Incidence Angle | Azimuth | Polarity |
|---|---|---|---|---|---|---|
| 378 | PLOR | 42:16.5 | 60.45 | 69 | 311 | c |
| 379 | ONER | 42:18.0 | 60.62 | 69 | 312 | c |
| 380 | ARR | 42:25.6 | 61.89 | 69 | 311 | c |
| 381 | CJR | 42:31.0 | 62.53 | 70 | 312 | c |
| 382 | MARR | 42:32.4 | 62.87 | 70 | 312 | c |
| 383 | DEV | 42:33.8 | 63.07 | 70 | 312 | c |
| 384 | SURR | 42:37.8 | 63.62 | 70 | 311 | c |
| 385 | RO20 | 42:38.0 | 63.67 | 70 | 311 | c |
| 386 | MFRD | 42:39.5 | 63.91 | 70 | 312 | c |
| 387 | BZS | 42:39.5 | 63.99 | 70 | 311 | c |
| 388 | MORH | 42:52.5 | 65.99 | 70 | 312 | c |
| 389 | KBS | 43:02.2 | 67.67 | 71 | 348 | c |
| 390 | KHC | 43:11.3 | 68.97 | 71 | 316 | c |
| 391 | CHTO | 58:12.6 | 4.28 | 44 | 139 | c |
| 392 | MKAR | 02:40.2 | 27.03 | 62 | 339 | c |
| 393 | NVS | 03:42.6 | 34.09 | 63 | 347 | c |
| 394 | BORK | 04:03.5 | 36.61 | 64 | 334 | c |
| 395 | SVE | 05:02.2 | 43.27 | 65 | 332 | c |

# REFERENCES


[1] Searle, M. P., Mitchell, A. H. G., Brown, R. D., & Szulc, A. G. (2007). The tectonic setting and evolution of the Shan Plateau, Myanmar. In *Tectonics of the Burma–Sunda Arc* (Vol. 321, pp. 47–68). *Geological Society, London, Special Publications*. https://doi.org/10.1144/SP321.3.

[2] Mitchell, A. H. G. (1993). Cretaceous–Cenozoic tectonic events in the Western Myanmar (Burma)–Assam region. *Journal of the Geological Society, 150*(6), 1089–1102. https://doi.org/10.1144/gsjgs.150.6.1089.

[3] Curray, J. R. (2002). Tectonics and history of the Andaman Sea region. Journal of Asian Earth Sciences, 20(3), 187–228.

[4] Hall, R. (2012). Late Jurassic–Cenozoic reconstructions of the Indonesian region and the Indian Ocean. *Tectonophysics, 570–571*, 1–41.

[5] Bertrand, G., & Rangin, C. (2003). Tectonics of the western margin of the Shan plateau (central Myanmar): Implication for the India-Indochina oblique convergence since the Oligocene. *Journal of Asian Earth Sciences, 21*(10), 1139–1157.

[6] Morley, C. K. (2002). A tectonic model for the Tertiary evolution of strike-slip faults and rift basins in SE Asia. *Tectonophysics, 347*, 189–215.

[7] Curray, J. R. (2005). Tectonics and history of the Andaman Sea region. *Journal of Asian Earth Sciences, 25*(2), 187–228. https://doi.org/10.1016/j.jseaes.2004.09.001.

[8] Rangin, C., Win Maw, San Lwin, Win Naing, Mouret, C., & Bertrand, G. (1999). Neotectonic evolution of the Indo-Burmese Range. *Marine Geology*.

[9] Kundu, B., & Gahalaut, V. K. (2012). Earthquake occurrence processes in the Indo-Burmese wedge and Sagaing fault region. *Tectonophysics, 524–525*, 135–146.

[10] Sloan, R. A., Jackson, J. A., McKenzie, D., & Priestley, K. (2017). India–Burma subduction in the northern Bay of Bengal. *Geophysical Journal International, 209*(1), 850–864.

[11] Uddin, A., & Lundberg, N. (2004). Miocene sedimentation and tectonics of the Bengal Basin. *Sedimentary Geology*.

[12] Bender, F. (1983). *Geology of Burma*. In D. Bannert (Ed.), *Beiträge zur Regionalen Geologie der Erde* (Vol. 16, pp. 1–261). Gebrüder Borntraeger.

[13] Mitchell, A. G. H., Chung, S.-L., Thura Oo, Lin, T.-H., & Hung, C.-H. (2012). Zircon U–Pb ages in Myanmar: Magmatic-metamorphic events and the closure of a Neo-Tethys ocean? *Journal of Asian Earth Sciences, 56*, 1–23.

[14] Soibam, I., Khuman, C.M., Subhamenon, S.S., (2015). Ophiolitic rocks of the Indo-Myanmar Ranges, NE India: Relicts of an inverted and tectonically imbricated hyper-extended continental margin basin? Geological Society, London, Special Publications, 413. doi:10.1144/SP413.12.

[15] Ghosh, A., et al. (2009). Tectonic significance of ophiolites in the Indo-Burma Ranges. *Gondwana Research*.

[16] Khuman, M.C., and Soibam, I., (2010). Ophiolite of Manipur its field setting and petrotectonic significance; Mem. Geol. Soc. India 75 255–290.

[17] Westerweel, J., Licht, A., Cogné, N., Roperch, P., Dupont -Nivet, G., Kay Thi, M., et al. (2020). Burma Terrane collision and northward indentation in the Eastern Himalayas recorded in the Eocene–Miocene Chindwin Basin (Myanmar). *Tectonics, 39*, e2020TC006413.

[18] Pivnik, D.A., Nahm, J., Tucker, R.S., Smith, G.O., Kyaw Nyein, Maungnyunt & Hla Maung, P. (1998). Polyphase deformation in a fore-arc/back-arc basin, Salin sub-basin, Myanmar (Burma). AmericanAssociation of Petroleum Geologists Bulletin, 82, 1837–1836.

[19] Cai, F., Ding, L., Zhang, Q., Orme, D. A., Wei, H., Li, J., Zhang, J. E., Zaw, T., & Sein, K. (2019). Initiation and evolution of

forearc basins in the Central Myanmar Depression. GSA Bulletin, 132, 1066–1082. https://doi.org/10.1130/B35301.1.

[20] Ridd, M. F., & Racey, A. (2015). Petroleum geology of Myanmar. *Geological Society, London, Memoirs, 45*, 1–6.

[21] Vigny, C., Socquet, A., Rangin, C., Chamot-Rooke, N., Pubellier, M., Bouin, M.-N., Bertrand, G., & Becker, M. (2003). Present -day crustal deformation around the Sagaing Fault, Myanmar. *Journal of Geophysical Research: Solid Earth, 108*(B11), 2533. https://doi.org/10.1029/2002JB001999.

[22] Socquet, A., Vigny, C., Chamot-Rooke, N., Rangin, C., Pubellier, M., Bouin, M.-N., Becker, M., & Charade, O. (2006). India and Sunda plates motion and deformation along their boundary in Myanmar determined by GPS. *Journal of Geophysical Research: Solid Earth, 111*(B5), B05406. https://doi.org/10.1029/2005JB003877.

[23] Tin Zin Htet, Vigny, C., Socquet, A., Ohnmar Myint, Myat Thura Aung, & Bertrand, G. (2022). Active deformation and strain partitioning around the Indo-Burma Range and Central Myanmar Basin from GPS data. *Journal of Geophysical Research: Solid Earth, 127*(6), e2021JB023759. https://doi.org/10.1029/2021JB023759.

[24] Curray, J. R., Moore, D. G., Lawyer, L. A., Emmel, F. J., Raitt, R. W., Henry, M., & Krishna, M. (1979). Tectonics of the Andaman Sea and Burma. In J. S. Watkins, L. Montadert, & P. W. Dickerson (Eds.), *Geology and petroleum resources of continental margins* (AAPG Memoir 29, pp. 189–198). American Association of Petroleum Geologists.

[25] Wang, P., Zhang, Y., & Li, D. (2011). The evolution of the deepwater sedimentary system in the Andaman Sea. *Marine Geology & Quaternary Geology, 31*(2), 49–56.

[26] Xiong, X., Wang, Y., Deng, Q., & Yu, W. (2017). Cenozoic evolution of the Sagaing Fault and its role in the tectonics of SE Asia. *Tectonophysics*, *721*, 408–423. https://doi.org/10.1016/j.tecto.2017.01.001.

[27] Tapponnier, P., Peltzer, G., Armijo, R., & Cobbold, P. (1986). On the mechanics of the collision between India and Asia. In M. P. Coward & A. C. Ries (Eds.), *Collision Tectonics* (Vol. 19, pp. 115–157). Geological Society, London, Special Publications. https://doi.org/10.1144/GSL.SP.1986.019.01.07.

[28] Maurin, T., & Rangin, C. (2010). Structure and kinematics of the Indo-Burma accretionary wedge: Recent and fast growth of the outer wedge. *Tectonics, 29*(5), TC2010. https://doi.org/10.1029/2009TC002514

[29] Xu, X. et al. (2016). Seismotectonic map in China and its adjacent regions (Seismogical Press).

[30] Wang, M., & Shen, Z.-K. (2020). Present-day crustal deformation of continental China derived from GPS and its tectonic implications. *Journal of Geophysical Research: Solid Earth, 125*, e2019JB018774.

[31] Zhang, P.-Z., et al. (2004). Continuous deformation of the Tibetan Plateau from global positioning system data. *Geology, 32*(9), 809–812.

[32] Engdahl, E. R. & Villaseñor, A. (2002). in International Geophysics Vol. 81 (eds William H. K. Lee, Hiroo Kanamori, Paul C. Jennings, & Carl Kisslinger) 665-cp662 (Academic Press).

[33] Willemann, R.J., Storchak, D.A., 2001. Data collection at the International Seismological Centre. Seismological Research Letters 72, 440–453. https://doi.org/10.1785/gssrl.72.4.440.

[34] Lentas, K., 2018. Towards routine determination of focal mechanisms obtained from first motion P-wave arrivals. Geophysical Journal International 212, 1665–1686. https://doi.org/10.1093/gji/ggx503.

[35] Lentas, K., Di Giacomo, D., Harris, J., Storchak, D.A., 2019. The ISC Bulletin as a comprehensive source of earthquake source mechanisms. Earth System Science Data 11, 565–578. https://doi.org/10.5194/essd-11-565-2019.

[36] Bormann, P., 1999. Take-off angle calculations for fault-plane solutions and reconstruction of nodal planes from the parameters of fault-plane solutions. GFZ. https://doi.org/10.2312/GFZ.NMSOP-2_EX_3.3.

[37] Bormann, P., Baumbach, M., 2012. Determination of fault-plane solutions by hand. GFZ. https://doi.org/10.2312/GFZ.NMSOP-2_EX_3.2.

[38] Kagan, Y.Y. (1991). 3-D rotation of double-couple earthquake sources. Geophys. J. Int., 106, 709-716.

[39] Kagan, Y.Y. (2005). Double-couple earthquake focal mechanism: random rotation and display, Geophysical Journal International, Volume 163, Issue 3, 1065–1072. https://doi.org/10.1111/j.1365-246X.2005.02781.x.

[40] Brune, J.N. (1970). "Tectonic Stress and the Spectra of Seismic Shear Waves from Earthquakes", Jour. Geophy. Res., Vol. 75, N 26, Pp 4997-5009.

[41] Brune, J.N. (1971). "Correction", Jour. Geophy. Res., Vol. 76, p 5002.

[42] Panda, D., Kundu, B., Gahalaut, V.K., Rangin, C. (2018). Crustal deformation, spatial distribution of earthquakes and along strike segmentation of the Sagaing Fault, Myanmar, Journal of Asian Earth Sciences, 166, 89-94. DOI: 10.1016/j.jseaes.2018.07.029.